



HAL
open science

Mineralogical and geochemical signatures of Quaternary pyroclasts alterations at the volcanic Trindade Island, South Atlantic

A.C.C. Mateus, A.F.D.C. Varajão, Sabine Petit, F.S. Oliveira, C.E.G.R. Schaefer

► To cite this version:

A.C.C. Mateus, A.F.D.C. Varajão, Sabine Petit, F.S. Oliveira, C.E.G.R. Schaefer. Mineralogical and geochemical signatures of Quaternary pyroclasts alterations at the volcanic Trindade Island, South Atlantic. *Journal of South American Earth Sciences*, 2020, 102, pp.102674. 10.1016/j.jsames.2020.102674 . hal-03001003

HAL Id: hal-03001003

<https://hal.science/hal-03001003>

Submitted on 30 Nov 2020

HAL is a multi-disciplinary open access archive for the deposit and dissemination of scientific research documents, whether they are published or not. The documents may come from teaching and research institutions in France or abroad, or from public or private research centers.

L'archive ouverte pluridisciplinaire **HAL**, est destinée au dépôt et à la diffusion de documents scientifiques de niveau recherche, publiés ou non, émanant des établissements d'enseignement et de recherche français ou étrangers, des laboratoires publics ou privés.

1 **Mineralogical and geochemical signatures of Quaternary pyroclasts** 2 **alterations at the volcanic Trindade Island, South Atlantic**

3
4 **A.C.C. Mateus^{a*}, A.F.D.C. Varajão^a, S. Petit^b, F.S. Oliveira^c, C.E. Schaefer^d**

5
6 ^aGeology Department, Universidade Federal de Ouro Preto, Campus Morro do
7 Cruzeiro, s/n, Ouro Preto, MG 35-4000-00, Brazil, anacamposeg@hotmail.com,
8 angelica@degeo.ufop.br

9 ^bInstitut de Chimie des Milieux et Matériaux de Poitiers (IC2MP), UMR7285CNRS,
10 Université de Poitiers, Poitiers, France, sabine.petit@univ-poitiers.fr

11 ^cGeosciences Institute, Geography Department, Universidade Federal de Minas Gerais,
12 Av. Antônio Carlos, 6627, Belo Horizonte, MG 31-270-901, Brazil,
13 fabiosolos@gmail.com

14 ^dSoil Science Department, Universidade Federal de Viçosa, Avenida Peter Henry Rolfs,
15 s/n, Viçosa, MG 36570-000, Brazil, carlos.schaefer@ufv.br

16 *Corresponding author: Ana Carolina Campos Mateus, anacamposeg@hotmail.com,
17 Tel: +55 35 3212-5310

18 19 20 **Abstract**

21 This paper reports the composition and alteration products of pyroclasts in the Holocene
22 Paredão volcano (pyroclast 1) and Late Quaternary Morro Vermelho Formation
23 (pyroclasts 2 and 3) of Trindade Island, South Atlantic, Brazil using combined
24 macromorphological, micromorphological, mineralogical and geochemical techniques.
25 The pyroclasts 1 and 2 are interpreted as volcanic tuff breccia deposits, whereas
26 pyroclast 3 is a lapilli deposit. They are dark gray in color with some altered reddish
27 regions and show vesicles and amygdaloid structures with small greenish crystals of 2.0
28 mm scattered throughout the matrix. The eruptions can be regarded as Strombolian-type
29 by producing pyroclastic deposits with coarse fragments with high vesicularity and
30 fluidal shape that indicate magmatic degassing and fragmentation. Petrologic and XRD
31 data revealed a mixture of biotite, goethite, ilmenite, anatase, magnetite, hematite,
32 pyroxene, zeolites, and olivine as their main mineral components. Optical microscopy
33 analysis confirms the vesicular and amygdaloid structures, with a hypocristalline
34 texture and a pale brown stained vitreous mass classified as sideromelane, due to its
35 basaltic composition. The sideromelane changes to a reddish brown and yellowish-
36 brown staining material identified as palagonite, clearly indicating a hydrovolcanic
37 eruption that occurs when the ascending magma comes into contact with water. Infrared
38 analyses in the palagonitized regions revealed the presence of halloysite, suggesting
39 alteration of sideromelane to tubular clay minerals. Amygdaloid and microfractures are
40 partially or totally filled with zeolites, which are formed by the percolation of water that
41 reacts with the palagonite and precipitation of chemical elements of hydrothermal fluid.
42 Reddish dark brown iddingsite and anhedral crystals of titaniferous magnetites occur in
43 the fractures and edges of the olivine. These crystals are also dispersed in the matrix
44 while some of them are zoned with Cr-rich core and Cr-poor edge, suggesting a deep
45 mantle origin of the magma. The high trace elements content can be related to
46 clinopyroxene (diopside) that include these elements. Geochemical data show that the
47 pyroclasts are undersaturated in silica, plotting in the ultrabasic and foidites fields on
48 the TAS classification diagram.

49
50 **Keywords:** Palagonite; Halloysite; Zeolites; Infrared

51 **1. Introduction**

52 The Trindade Island is a small Brazilian island of $\sim 13 \text{ km}^2$ and located in the South
53 Atlantic (Fig. 1). The Island is part of an extensive east-west-oriented underwater
54 volcanic chain, called Vitória-Trindade, and constitutes the upper portion of a volcanic
55 building of $\sim 5.2 \text{ km}$ high. The Vitória-Trindade Chain corresponds to the western
56 extension of the Trindade Victory Fracture Zone, located at $18^\circ 40'$ in the Mid Atlantic
57 Ridge (Alves et al., 2006). The Island is formed by five different volcanic episodes of
58 lava flows and intrusions of poor silica rocks with accentuated sodium-alkaline content
59 (Almeida, 1961). These volcanic episodes were described by Almeida (1961) from
60 bottom to top as: Trindade complex, Desejado sequence, Morro Vermelho Formation
61 (MV), Valado Formation and Vulcão do Paredão Formation (VP) (Fig.1). The volcanic
62 spills are overlain by the Holocene deposits that represent a small portion of the
63 stratigraphic units occurring on the island (Castro and Antonello, 2006) (Fig.1).
64 Particularly in MV and VP formations, there are several pyroclasts such as lapilli and
65 ash tuffs containing rotational lumps, blocks, aggregates and agglutinates of
66 melaneferintic, basanite and tephritic lava. Cordani (1970) suggested an eruption age by
67 potassium-argon dating method of 0.17 Ma for the MV deposits. However, Pires et al.
68 (2016) recorded a 0.25 Ma age for the VP volcanic deposits and suggests that this
69 volcanism represents the most recent volcanic activity of the Brazilian territory.

70 Studies of volcano stratigraphy and eruption geological models in the area of the
71 Paredão Volcano (Pasqualon, 2017) and Morro Vermelho Formation (Luz, 2016)
72 showed intercalation of nephelinitic flows and pyroclastic deposits, leading to the
73 interpretation of heterogeneous volcanism characterized by an early stage of the
74 Hawaiian style eruption (Sumner et al., 2005; Parcheta et al., 2012; Rader et al., 2015),
75 and a final phase of the Strombolian style. According to Pasqualon (2017) and Luz
76 (2016), the Hawaiian style is represented, in the study area, exclusively by a'a flows but
77 without describing the a'a morphotypes (Murcia et al., 2014). The Strombolian style is
78 represented by pyroclasts deposits of tuff breccia and lapilli being composed mainly of
79 basaltic scoria (Pasqualon, 2017 and Luz, 2016).

80 The petrological and geochemical studies of the olivine-nephelinites in the VP rocks
81 showed strongly fractionated REE patterns in the melaneferinites and basanites–
82 tephrites, suggesting the presence of garnet as a probable residual phase and generation
83 of melt at about 100 km depth (Marques et al., 1999). Bongiollo et al. (2015) recently

84 used geochemical modeling to show that the nephelinites in Trindade Island were from
85 magmas derived at a minimum of 1490 °C and 3 Gpa (>100 km depth).

86 Studies to date have focused on the petrogenesis and age of lava flows and intrusions on
87 Trindade Island.

88 Except for studies of alteration of olivine crystals of the pyroclasts (Mateus et al., 2018),
89 there is still a deficiency of studies with emphasis on alteration of the rocks, that evolve
90 specific factors like young volcanic parent materials, interaction with seawater and
91 climate conditions. Detailed studies analyzing the features of palagonization and
92 zeolitization, which are constantly found on oceanic islands with basic rocks consisting
93 of sideromelane altered to palagonite (Wentworth, 1926; Stearns and Vaksvik, 1935;
94 Nakamura, 1961; Einarsson, 1965; Thorseth et al., 1991) and to zeolite (Nayudu, 1964;
95 Hay and Iijima, 1968; Iijima and Harada, 1969; Kristmannsdóttir and Tómasson, 1978),
96 can be used to understand the mechanisms involved in the transformations of pyroclastic
97 rocks from the Trindade Island.

98 Therefore, this study used combined macromorphological, micromorphological,
99 mineralogical and geochemical techniques to examine the composition, alteration
100 products, and origin of the pyroclasts in MV and VP formations.

101 **2. Methodology**

102 The pyroclastic rocks were collected from the Holocene VP Formation (the latest event)
103 and the Late Quaternary MV formation. Macromorphologically, the coloration and the
104 mineral constituents of the rocks were observed with the aid of a magnifying glass of
105 20x. The pyroclasts were measured and classified according to the systematic of the
106 IUGS (Le Maître, 2002) taking into account the size of the clasts. The petrological
107 description including mineralogy, texture, estimation of the percentage of minerals and
108 photographic images were performed in polished thin sections using a Zeiss microscope
109 coupled with a camera.

110 More detailed mineralogical information was obtained on the samples using X-Ray
111 Diffraction (XRD) technique. The samples were initially gently powdered in agate
112 mortar and sieved with 250 mesh. The samples were analyzed at a scanning interval of 2
113 to 70 °2θ with a step size of 0.02 ° 2θ/s using a CuKα radiation and power 45KV and
114 40mA on a Panalytical diffractometer at the Universidade Federal de Ouro Preto
115 (DEGEO/UFOP), Brazil. The diffractograms were interpreted with X'pert HighScore

116 Plus software and compare with standards (Brindley and Brown, 1980). The Transform
117 Fourier Thermo Nicolet, Nexus 5700 series infrared spectrometer coupled with
118 Thermo Scientific Nicolet Continuum microscope was used to complement the XRD
119 mineralogical analyses at the IC2MP institute, Université de Poitiers, France. These
120 analyses were performed on clay fractions and point analyses in thin sections. In
121 microscope the near-infrared spectra ($8000\text{-}4000\text{ cm}^{-1}$) were obtained using source of
122 white light, beamsplitter CaF_2 , resolution of 4 cm^{-1} , optical velocity of 0.3165 cm s^{-1} and
123 100 scans. The spectra of clay fraction were obtained with the same condition of
124 acquisition in thin sections, but with velocity of 0.12659 cm s^{-1} .

125 Image analyses of the clay minerals were performed with a JEOL 2011 Bruker Esprit
126 Transmission Electron Microscope (TEM) at CinaM-CNRS, Aix Marseille University.
127 The suspended clay separates were deposited onto carbon coated Formvar film Cu
128 grids. The palagonitized regions were scraped and then deposited in resin to be made
129 cuts in ultramicrotome. The cuts were deposited in grids.

130 The chemical analyses of the major and trace element compositions of the samples were
131 measured in the ICP-OES Agilent Technologies 725 while the rare earth elements
132 (REE) were performed in the ICP-MS Agilent Technologies 7700 at DEGEO/UFOP
133 LGqa Laboratory. For total digestion of 0.1g of each sample, 1ml of hydrogen peroxide,
134 3ml of HCl at 10mol/L, 6 ml of HNO_3 to 10mol/L, 20ml of HNO_3 to 2 mol/L and 4ml
135 of HF concentrate were used. The percentage of SiO_2 was calculated in a relative way
136 by the difference to 100% in the sum of the main elements and LOI.

137 Back-scattered electron images and semi-quantitative chemical analyses by Electron
138 Dispersive X-ray (EDX) were made to analyze the habit and chemical compositions,
139 respectively, of the volcanic glass and palagonite. These analyzes were made in
140 Scanning Electron Microscope (SEM) coupled with EDX Jeol JSM-6510 with an
141 operating voltage of 20KV.

142 The microanalyses of the olivines, pyroxenes, zeolites, spinels, sideromelane and
143 palagonite were performed with electron microprobe JEOL JXA-8230 at the
144 Microanalysis Laboratory of the DEGEO/UFOP. The acceleration and current
145 conditions were 15 kV and 20 nA, and corrections of the common ZAF matrix were
146 applied. The counting time in the peaks/background were 10/5s for all elements except
147 the sodium that was 20/10s (Na, Si, Al, Mg, Fe, Cr, Ti, Ca, Ni, K, Mn). The punctual
148 analyses were calibrated with jadeite-TAP, rutile-LIF, sanidine-PETJ, magnesium-TAP

149 oxide, chromium-LIF oxide, AN100-PETJ, corindon-TAP, rodonite-LIF, quartz-TAP,
150 magnetite-LIF. The FeO was considered as the amount of total iron obtained through
151 the microprobe.

152 **3. Results**

153 The pyroclastic rocks collected in the VP (pyroclast 1) and MV formations (pyroclasts 2
154 and 3) were classified according to their sizes (Le Maître, 2002). The pyroclasts 1 and 2
155 are classified as tuff breccia deposit according to diagram of Németh and Martin (2007).
156 The pyroclasts 1 and 2 contain more than 75% of angular and subangular fragments
157 larger than 64.0mm (blocks) (Figs. 2A, C). In addition, pyroclast 1 contains fragments
158 between 2.0 and 64.0mm (lapilli; Fisher, 1966) in smaller proportions (Fig. 2B). The
159 pyroclast 3 belongs to a lapilli deposit containing more than 75% of 2.00 to 64.00mm
160 (lapilli) fragments (Figs. 2D, E). Macroscopically, all the pyroclasts have dark gray
161 color with some brownish to reddish regions, and vesicular and amygdaloid structures
162 (Fig. 2). The matrix of the pyroclasts contain scattered small green crystals (~2.0 mm).
163 Owing to the fine-grained size (<1.0 mm) of the matrix constituents, it is difficult to
164 distinguish their mineral composition in macroscopic view.

165 Microscopically the pyroclast 1 are altered and show reddish brown vitreous matrix
166 (Fig. 3A) that is attributed to exposure to intense alteration. Some regions of pyroclasts
167 2 have grayish stains because of the presence of unaltered portions of the rock (Fig. 3E).
168 However, fragments in pyroclast 3 are yellowish brown in color (Fig. 3J). All the
169 pyroclasts have vesicular and amygdaloid structures and hypocrySTALLINE textures (Figs.
170 3A, D, J). The pyroclasts are composed of a pale brown vitreous mass in 50% of thin
171 section area, which are isotropic in crossed polarized light and occurs around olivine,
172 pyroxene and spinel crystals. Bulk rock XRD analyses show that the matrix of these
173 pyroclasts are essentially composed of biotite, goethite, ilmenite, anatase, magnetite,
174 hematite, pyroxene and olivine (Mateus et al., 2018).

175 *Glass* – The vitreous mass (glass) is classified as sideromelane due to the basaltic
176 composition of the pyroclasts (Table 1; Figs. 4B, C). The sideromelane changes to a
177 reddish brown (Fig. 3B) and yellowish brown (Fig. 3K) materials identified as
178 palagonites. In pyroclast 1, the glass is totally palagonitized and it is possible to find
179 only sideromelane in pyroclasts 2 and 3. The reddish colorations are due to a high
180 degree of alteration and high Fe content. In some portions, palagonite is whitish (Fig.
181 3K) due to leaching of Fe in the reddish brown and yellowish brown palagonite. This

182 process is similar to what was observed in palagonites of Iceland (Thorseth et al., 1991).
183 Chemical analyses of the palagonite showed a loss of alkali and alkaline-earth elements
184 (Na, Ca, Mg) and enrichment of Fe and water in relation to the sideromelane (Table 1)
185 in the reddish and yellowed regions. This composition is similar to those found in
186 palagonites from previous studies such as Peacock (1926, 1928), Thorseth et al. (1991),
187 Stroncik and Schmincke (2001, 2002) and Pauly et al. (2011). The infrared analyses in
188 the palagonitized regions of pyroclasts 1 and 2 showed the presence of halloysite (Fig.
189 5). Notably, the characteristic bands of halloysite are observed at about 7070, 7200, and
190 4530 cm^{-1} . The two former bands are attributed to the first overtones of the Al_2OH
191 stretching vibrations and the latter band to the Al_2OH stretching plus bending
192 combination mode (Madejová et al., 2011). Images of TEM confirm the presence of
193 tubular halloysite in the clay fraction of the altered and palagonitized portions of the
194 pyroclasts. The diameter of the tubes ranges from 0.1 to $0.2\mu\text{m}$ (Fig. 6). Figure 6B
195 shows a halloysite crystal and a fragment of volcanic glass.

196 *Olivine* – Olivine is euhedral, forsterite (Fo_{80}) in composition (Mateus et al., 2018) and
197 makes up 20% of the rock in all the pyroclasts. The olivine phenocrysts in pyroclast 1
198 are essentially altered and fractured with axis sizes greater than 1mm (Fig. 3A). The
199 fractures and edges of these altered and fractured olivine phenocrysts in pyroclasts 1 are
200 filled and corroded with reddish dark brown colored iddingsite (Fig. 3A). However,
201 well preserved olivine phenocrysts with sizes ranging from 0.5mm to 3mm dominate
202 pyroclasts 2 and 3 (Figs. 3D, L).

203 *Pyroxene* – The pyroxenes were observed as very small crystals about of $70\mu\text{m}$ in the
204 form of microliths in the vitreous matrix and present in trace amount (5 %) in pyroclast
205 1 (Fig. 3B). Pyroxenes in pyroclast 2 are mostly tiny ($20\mu\text{m}$), dispersed in the matrix
206 and surround the olivine phenocrysts with high interference colors, and are present in
207 small amount (15 %). However, largest crystals of $\square 120\text{mm}$ are rarely found (Fig. 3F).
208 In the pyroclast 3, prismatic pyroxenes, constituting about 25 %, are tiny ($\square 20\mu\text{m}$) and
209 occur within the microlytic matrix and surrounding the olivine phenocrysts (Fig. 3L).
210 Electron microprobe micro-chemical analyses show that the pyroxene in pyroclasts 1
211 and 2 are diopside (Table 2; Fig. 7). TEM analyses also show occurrence of fragments
212 of pyroxene in clay fraction (Fig. 6D).

213 *Spinels* – Spinels are commonly observed dispersed in the matrix of the pyroclasts, and
214 within the fractures and edges of olivine phenocrysts in varying trace amounts (5 – 10

215 %; Fig. 3C). The crystals are anhedral and are about 0.05mm in size. Electron
216 microprobe analyses shows that the spinels are titaniferous magnetites, and some
217 crystals display Cr-rich and Cr-poor zones (Table 3; Figs. 4E, G, H). Due to the degree
218 of alteration of the spinels, it was difficult and nearly impossible to determine their
219 chemical composition as none of the analysis was close to 100 %.

220 *Zeolite* – In pyroclast 2, amygdales and microfractures are partially to completely fill by
221 zeolites (Figs. 3D, E, H). The zeolites are small pseudorhomboidal crystals (Fig. 3E),
222 mostly less than 20 μm , with low interference colors, and constitute about 10% in thin
223 section observations. The zeolites filled microfractures sometimes crosscut the olivine
224 crystals (Figs. 3G, I) and vesicles (Fig. 3I), suggesting their latter and secondary
225 crystallization. The zeolites also crystallize in the walls of the palagonitized portions
226 (Fig. 4F).

227 Electron microprobe analyses of the zeolites in pyroclast 2 shows that they are
228 predominantly heulandite-Ca and chabazite-Ca (Table 4; Figs. 4F, G). Both the
229 heulandite-Ca and chabazite-Ca are found in the amygdales filled zeolites while those in
230 the microstructure veins are essentially chabazite-Ca. The average calculated structural
231 formula is $(\text{Ca}_{3.17}\text{Na}_{0.85}\text{K}_{4.28})_{8.3}(\text{Si}_{21.58}\text{Al}_{10.34})\text{O}_{72}.26\text{H}_2\text{O}$ and $\text{Ca}_{1.31}(\text{A}_{14.42}\text{Si}_{7.6}\text{O}_{24}).13\text{H}_2\text{O}$
232 for the heulandite-Ca and chabazite-Ca, respectively. The Si:Al ratios are relatively low
233 in the heulandite-Ca (2.08) and chabazite-Ca (1.74).

234 *Geochemical of pyroclasts* – The pyroclasts are undersaturated with silica (~37 %).
235 Na_2O content is higher than K_2O in pyroclasts 1 and 2 but lower in pyroclast 3 (Table
236 5). All the pyroclasts plot in the ultrabasic rocks and foidites fields on the $\text{Na}_2\text{O} + \text{K}_2\text{O}$
237 vs SiO_2 TAS classification diagram (Fig. 8; Les Bas et al., 1986). The high FeO, MgO,
238 TiO_2 and CaO contents in all the pyroclasts (Table 5) are probably due to the presence
239 of ferromagnesian minerals such as magnetites, olivines, ilmenites and clinopyroxene.
240 The pyroclasts are also enriched in trace elements, such Ba, Cr, Sr, V, Zr, Zn and Ce
241 (Table 5). The elevated trace elements contents are related to the presence of pyroxenes
242 as shown by Panina and Stoppa (2009) who documented the enrichments of trace
243 elements in clinopyroxenes in foidian olivine in southern Italy. Moreover, the pyroclasts
244 display strong enrichments of light rare earth elements (LREE) over the heavy rare earth
245 elements (HREE) ($\sum\text{LREE}/\sum\text{HREE} = 12.38$ to 13.71 ; $\text{La}/\text{Yb} = 33.55$ to 40.85 , Table 5.5
246 and Fig. 9).

247 **4. Discussions**

248 **4.1 The eruption type and the alteration process of pyroclasts**

249 According to Walker and Croasdale (1971), the eruptions during the formation of
250 pyroclastic deposits can be regarded as Strombolian-type by producing initially coarse
251 materials, with a restricted range of sizes. This affirmation is attested in this study by
252 the presence of blocks and lapilli. Additionally, the high vesicularity and fluidal shape
253 presented by the fragments, that indicate degassing and magmatic fragmentation, are
254 characteristic of Strombolian-type eruption (Vergnolle and Brandeis, 1996; Vergnolle
255 et al., 1996; Houghton et al., 1999). The Strombolian-type eruption is supported by
256 studies of Pasqualon (2017) and Luz (2016) on pyroclasts deposits in the areas of this
257 study.

258 The main alteration products of pyroclasts are: palagonite, iddingsites, halloysite and
259 zeolites.

260 The palagonite is an alteration product of volcanic glass (like sideromelane) and its
261 presence is characterized by regions with reddish and yellowish color due to the relative
262 concentration of iron due to the loss of more mobile chemical elements such as Na, K,
263 Mg (Stroncik and Schimincke, 2002). Several authors consider that the palagonite is
264 the first stable product of aquatic mafic glass alteration (Peacock, 1926; Hay and Iijima,
265 1968; Staudigel and Hart, 1983; Furnes, 1984; Thorseth et al., 1991). Bunsen (1847)
266 and Correns (1930) were the first to observe that the alteration of sideromelane to
267 palagonite results in loss of some elements. An explanation for the formation of
268 palagonite would be a hydrovolcanic eruption that occurred when the ascending magma
269 came into contact with sea water at high tide (Stroncik and Schimincke, 2001). The
270 process of palagonitization by the hydrovolcanic eruption (Németh and Kósik, 2020)
271 has been previously described in volcanic islands, such as the Azores, Hawaii
272 (Wentworth, 1926; Stearns and Vaksvik, 1935) and Oshima (Nakamura, 1961); and in
273 lakes or low ground with a high groundwater in Auckland (Searle, 1965), Idaho
274 (Hamilton and Bvers, 1963) and Iceland (Einarsson, 1965). According to Bonati (1965),
275 hydration of the lava is probably faster at higher temperatures when the lava is still in a
276 molten state. During this phase, the hydrous lava forms directly hydrated glass
277 (palagonite). This process seems to have occurred in the pyroclast 2 because there is a
278 large amount of yellowish brown palagonite with little sideromelane.

279 Following the complete consolidation of magma and the alteration of volcanic glass as a
280 result of seawater interaction, the pyroclasts underwent a second phase of alteration due

281 to exposure to meteoric water. The presence of halloysite in the palagonitized
282 sideromelane attested by infrared and MET analyses; the crystals of olivine and
283 amigdals cut by zeolites veins, the presence of zeolites crystallized in palagonitized
284 regions; and the presence of iddingsitized olivines (see Mateus et al., 2018) corroborate
285 this proposition.

286 Alterations of sideromelane to zeolites have been described in palagonite tuffs from
287 Oahu, Hawaii (Hay and Iijima, 1968; Iijima and Harada, 1969) and Iceland (Nayudu,
288 1964). The probable formation of zeolites in pyroclast 2 would be the reaction of
289 sideromelane with meteoric fluid in temperature around of 100°C. According to
290 Kristmannsdóttir and Tómasson (1978), heulandite, stilbite and analcime may form at
291 temperatures below 100°C. Barrows (1980) described heulandite, clinoptilolite,
292 mordenite, analcime, thomsonite, erionite and chabazite in thick Miocene volcanoclastic
293 sequences in Nevada attributed to a process involving the circulation of low temperature
294 meteoric fluid in an open hydrologic system. Höller and Wirsching (1980) observed the
295 formation of chabazite, phillipsite, and analcime in the reaction of nephelinite with a
296 solution of 0.01 N NaOH at 150°C in open system.

297 In this study, the meteoric water reacted with the vitreous matrix of the rock to form the
298 palagonite and precipitated the Si, Al, Ca, Na, and K in the form of zeolites in the
299 adjacencies of the palagonite, similar to the one described by Hay and Iijima (1968) and
300 Iijima and Harada (1969) in zeolithic palagonite tuffs. The occurrence of zeolites
301 impoverished in silica is due to the low silica contents in the pyroclasts and primary
302 basaltic magma.

303 In all pyroclasts occur olivines iddingsitized by meteoric water. The difference in the
304 degree of preservation or alteration of olivine phenocrysts between VP (pyroclast 1) and
305 MV (pyroclasts 2 and 3) is related to their position on the sampling profile (Mateus et
306 al., 2018). The pyroclast 1 was collected at higher altitude and in a more humid region,
307 exposing it to greater leaching and alteration processes compared to pyroclasts 2 and 3
308 that were collected from much lower altitude with less exposure to alterations. Mateus
309 et al. (2018) argue that the presence of iddingsite in the high altitude and humid region
310 indicates an advanced alteration stage of the olivine crystals during weathering.

311 **4.2 Geochemical considerations**

312 The presence of spinels enriched with chromium and the LREE enrichment indicate that
313 the magma has a mantelic origin (Irvine, 1965).

314 The strongly fractionated REE patterns suggest the presence of garnet as a probable
315 residual phase, implying that melt generation occurred at depths of about 100 km. This
316 interpretation is corroborated by the earlier work of Marques et al. (1999), who
317 suggested a garnet magma source at deeper depth (~100 km) for the olivine-nephelinites
318 in the VP Formation and proven by Bongiollo et al. (2015) through geochemical
319 modeling.

320 **5. Conclusions**

321 The Quaternary pyroclastic rocks of the Vulcão do Paredão (Holocene) and Morro
322 Vermelho (Pleistocene) showed the following products of alteration:

323 1- sideromelane palagonitized through the interaction of magma with the sea water and
324 subsequently with meteoric water;

325 2- particularly in the pyroclast 2, the palagonite alters to form zeolite and halloysite
326 through the passage of hydrothermal fluids and meteoric water during weathering.

327 The main factors justifying this assertion are:

328 1- in the palagonitized regions there is a loss of bases (Na, Ca, Mg) and an enrichment
329 of Fe and water in relation to the sideromelane;

330 2.1- the chemical analysis by microprobe showed the presence of zeolites alongside the
331 palagonite;

332 2.2- the point-source analyses of infrared allow to identify halloysite in the palagonite
333 of pyroclast with totally altered sideromelane;

334 2.3- TEM observations confirm the presence of halloysite in the palagonitized regions.

335 In addition, the presence of palagonite may indicate a hydrovolcanic eruption for these
336 deposits.

337 **Acknowledgements**

338 Special thanks to the Brazilian Navy for their logistical support and to the CNPq
339 (306424/2016-9; 442730/2015-2), CAPES (scholarship) and FAPEMIG (PPM- 00326-
340 18) and the European Union (ERDF) and Région Nouvelle Aquitaine for their financial
341 contribution. We would also like to express our gratitude to Olivier Grauby (CINam-

342 CNRS - Aix Marseille University) for assistance in the TEM observations, the
343 Microanalysis Laboratory of the Universidade Federal de Ouro Preto, member of the
344 Microscopy and Microanalysis Network of Minas Gerais State/Brazil/FAPEMIG and to
345 the Laboratory of Microanalysis and Electronic Microscopy of the Microscopy Center
346 of the Universidade Federal de Minas Gerais for the mineral chemical analyses. Lastly,
347 we would like to show our appreciation to the Laboratory of X-Ray Diffraction of
348 DEGEO/UFOP DRX and laboratory IC2MP, Université de Poitiers for the
349 mineralogical analyses. The authors would like to thank the reviewers Karoly Nemeth
350 and Sorin C. Barzoi, who greatly improved our manuscript.

351 **References**

- 352 Almeida, F.F.M., 1961. Geologia e petrologia da Ilha de Trindade. Serviço Gráfico
353 do Instituto Brasileiro de Geografia e Estatística, Rio de Janeiro, 197 p.
- 354 Alves, E.C., Maia M., Sichel S.E., Campos, C.M.P., 2006. Zona de Fratura de
355 Vitória-Trindade no oceano atlântico sudeste e suas implicações tectônicas. Rev.
356 Bras. Geofís. 24(1),117–127.
- 357 Barrows, K.J.,1980. Zeolitization of Miocene volcanoclastic rocks, southern
358 Desatoya Mountains, Nevada. Geol. Soc. Am. Bull. 91,199–210.
- 359 Bonatti, E., 1965. Palagonite, hyaloclastites and alteration of volcanic glass in the
360 Ocean. Bull. Volcanol. 28(1), 257–269.
- 361 Bongioiolo, E.M., Pires, G.L.C., Geraldés, M.C., Santos, A.C., Neumann, R., 2015.
362 Geochemical modeling and Nd–Sr data links nephelinite–phonolite successions and
363 xenoliths of Trindade Island (South Atlantic Ocean, Brazil). J. Volcanol. Geotherm.
364 Res. 306, 58–73.
- 365 Brindley, G.W., Brown, G., 1980. Crystal Structures of Clay Minerals and Their X-
366 ray Identification. Mineralogical Society, London, 495 p.
- 367 Bunsen, R.,1847. Beitrag zur Kenntnis des isländischen Tuffgebirges. Ann. Chem.
368 Pharm. 61, 265–279.
- 369 Castro, J.W.A., Antonello, L.L., 2006. Geologia das ilhas oceânicas brasileiras. In:
370 Alves, R.J.V., Castro, J.W.A. (Eds.), Ilhas Oceânicas Brasileiras: da Pesquisa ao
371 Manejo. Ministério do Meio Ambiente, Brasília, pp. 29–57.

- 372 Cordani, U. G. 1970. Idade do vulcanismo do Oceano Atlântico Sul. São Paulo:
373 Instituto de Geociências e Astronomia. Boletim IGA, 1, 9–75.
- 374 Correns, C. W., 1930. Über einen Basalt vom Boden des atlantischen Ozeans und
375 seine Zersetzungsrinde. Chem. Erde. 5, 76– 86.
- 376 Einarsson, T., 1965. The ring-mountains Hverfiall, Lúdent, and Hrossaborg in
377 northern Iceland. Vísindafélag Íslendinga, Greinar 41, 1–28.
- 378 Fisher, R.V., 1966. Rocks composed of volcanic fragments. — Earth Science Review
379 1, pp. 287–298.
- 380 Furnes, H., 1984. Chemical-changes during progressive subaerial palagonitization of
381 a subglacial olivine tholeiite hyaloclastite – a microprobe study. Chem. Geol. 43,
382 271–285.
- 383 Hamilton, W., Bvers, W.B., 1963. Menan Buttes, cones of glassy basalt tuff in the
384 Snake River Plain, Idaho. U. S. Geol. Surv. 450-E, 114–118.
- 385 Hay, R.L., Iijima, A., 1968. Petrology of Palagonite Tufts of Koko Craters, Oahu,
386 Hawaii. Contr. Mineral. and Petrol. 17, 141–154.
- 387 Höller, H., Wirsching, U., 1980. Experiments on the hydrothermal formation of
388 zeolites from nepheline and nephelinite. Proc. 5th Int'l Conf on Zeolites, Heyden,
389 London, pp. 164–170.
- 390 Houghton, B.F., Wilson, C.J.N., Smith, I.E.M., 1999. Shallow-seated controls on
391 styles of explosive basaltic volcanism: a case study from New Zealand. J. Volcan.
392 Geoth. Res. 91 (1), 97–120.
- 393 Iijima, A., Harada, K., 1969. Authigenic zeolites in zeolitic palagonite tuffs on Oahu,
394 Hawaii. Am. Mineral. 54, 182–197.
- 395 Irvine, T.N., 1965. Chromian spinel as a petrogenetic indicator. Part. 1. Theory.
396 Canad. J. Earth Sci. 2, 648–672.
- 397 Kristmannsdóttir, H., Tómasson, J., 1978. Zeolite zones in geothermal areas, Iceland.
398 In: Sand, L.B., Mumpton, F.A. (Eds.), Natural Zeolites. Pergammon Press, Oxford,
399 pp. 277–284.

400 Le Bas, M.J., Le Maître, R.W., Streckeisen, A., Zanettin, B., 1986. A chemical
401 classification of volcanic rocks based on the total alkali–silica diagram. *J. Petrol.*
402 27,745–750.

403 Le Maître, R.W., Batema, N.P., Dudek, A., Keller, J., Lameyre, J., Le Bas, M.J.,
404 Sabine P.A., Schmid, R., Sorensen, H., Streckeisen, A., Woolley, A.R., Zanettin, B.,
405 2002. *Igneous Rocks: A Classification and Glossary of terms*. Cambridge University
406 Press, New York, 236 p.

407 Luz, F. R., 2016. *Estudo do Vulcanismo da Ilha da Trindade: estratigrafia e*
408 *petrologia da Formação Morro Vermelho*. Monography, Porto Alegre, Instituto de
409 Geologia/Universidade Federal do Rio Grande do Sul, 112p.

410 Madejová, J., Balan, E., Petit, S., 2011. Application of vibrational spectroscopy to the
411 characterization of phyllosilicates and other industrial minerals. In: Christidis, G.E.
412 (Ed.), *Advances in the characterization of industrial minerals*, EMU Notes in
413 Mineralogy. European Mineralogical Union and Mineralogical Society of Great
414 Britain and Ireland, Cambridge, pp.171–226.

415 Marques, L.S., Ulbrich, M.N.C., Ruberti, E., Tassinari, C.G., 1999. Petrology,
416 geochemistry and Sr-Nd isotopes of Trindade and Martin Vaz volcanic rocks
417 (Southern Atlantic Ocean). *J. Volcan. Geoth. Res.* 93, 191–216.

418 Mateus, A.C.C., Varajão, A.F.D.C., Oliveira, F.S., Schaefer, C.E., 2018. Alteration of
419 olivine in volcanic rocks from Trindade Island, South Atlantic. *Appl. Clay Sci.* 160,
420 40–48.

421 Morimoto, M., 1988. Nomenclature of pyroxenes. *Min. Mag.* 52, 535–550.

422 Murcia, H., Németh, K., Moufti, M.R., Lindsay, J.M., El-Masry, N., Cronin, S.J.,
423 Qaddah, A., Smith, I.E.M., 2014. Late Holocene lava flow morphotypes of northern
424 Harrat Rahat, Kingdom of Saudi Arabia; implications for the description of
425 continental lava fields. *J. Asian Earth Sci.* 84, 131–145.

426 Nakamura, K., 1961. Stratigraphic studies of the pyroclastics of Oshima Volcano de-
427 posited during the last fifteen centuries. II. Activity of parasitic volcanoes. *Sci. Pap.*
428 *Coi. Gen. Educ., Univ. Tokyo* 11, 281–319.

429 Nayudi, Y.R., 1964. Palagonite tufts (hyaloclastites) and the products of post-eruptive
430 processes. *Bull. Volcanol.* 27, 391–410.

431 Németh, K., Martin, U., 2007. Practical volcanology - Lecture notes for
432 understanding volcanic rocks from field based studies. Geological Institute of
433 Hungary, Budapest, 221p.

434 Németh, K., Kósik, S., 2020. Review of Explosive Hydrovolcanism. *Geosciences*
435 10(2), 44.

436 Panina, L.I., Stoppa, F., 2009. Silicate-carbonate-salt liquid immiscibility and origin
437 of the sodalite-haüyne rocks: study of melt inclusions in olivine foidite from Vulture
438 volcano, S. Italy. *Cent. Eur. J. Geosci.* 1(4), 377–392.

439 Parcheta, C.E., Houghton, B.F., Swanson, D.A., 2012. Hawaiian fissure fountains 1:
440 decoding deposits-episode 1 of the 1969-1974 Mauna Ulu eruption. *Bull. Volcanol.*
441 74(7), 1729–1743.

442 Pasqualon, N. G., 2017. Estratigrafia, petrologia e padrões de porosidade dos
443 depósitos do Vulcão do Paredão, Ilha da Trindade, Brasil. Monography, Porto Alegre,
444 Instituto de Geologia/Universidade Federal do Rio Grande do Sul, 143p.

445 Patrício, R.L., 2012. Mapeamento da Ilha de Trindade, Atlântico Sul. Monografia,
446 Universidade Estadual Paulista, Brasil, 59p. (in Portuguese, with English Abstr.).

447 Pauling, B.D., Schiffman, P., Zierenberg, R.A., Clague, D.A., 2011. Environmental
448 and chemical controls on palagonitization. *Geochem. Geophys. Geosyst.* 12 (12), 1–
449 26.

450 Peacock, M.A., 1926a. The palagonite formation of Iceland. *Geol. Mag.* 63, 385–399.

451 Peacock, M.A., 1926b. The geology of Videy, southwest Iceland; a record of igneous
452 action in Glacial times. *Trans. R. Soc. Edinburgh* 5A, 441–465.

453 Peacock, M.A., 1926c. The petrology of Iceland, part I. The basic turfs. *Trans. Roy.*
454 *Soc. Edinburgh* 55, 51–76.

455 Peacock, M.A., Fuller, R.E., 1928. Chlorophaeite, sideromelane, and palagonite from
456 the Columbia River Plateau. *Am. Mineral.* 13, 360–382.

457 Pires, G.L.C., Bongioiolo, E.M., Geraldés, M.C., Renac, C., Santos, A.C., Jourdan, F.,
458 Neumann, R., 2016. New $^{40}\text{Ar}/^{39}\text{Ar}$ ages and revised $^{40}\text{K}/^{40}\text{Ar}^*$ data from
459 nephelinitic-phonolitic volcanic successions of the Trindade Island (South Atlantic
460 Ocean). *J. Volcanol. Geotherm. Res.* 327, 531–538.

461 Rader, E., Geist, D., 2015. Eruption conditions of spatter deposits. *J. Volcanol.*
462 *Geotherm. Res.* 304, 287–293.
463

464 Searle, E.J., 1965. Auckland volcanic district in New Zealand volcanology.
465 Northland, Coromandel, Auckland. *New Zeal. Geol. Surv. Handb., Info. Ser.* 49, 90–
466 103.

467 Staudigel, H., Hart, S.R., 1983. Alteration of basaltic glass: mechanisms and
468 significance for the oceanic crust-sea water budget. *Geochim. Cosmochim. Acta* 47,
469 337–350.

470 Stearns, H.T., Vaksvik, K.N., 1935. Geology and ground-water resources of the
471 island of Oahu, Hawaii. *Hawaii Division of Hydrography Bulletin* 1, U. S. Geological
472 Survey, Hawaii, 479 p.

473 Stroncik, N.A., Schimincke, H.U., 2001. The evolution of palagonite: crystallization,
474 chemical changes, and element budget. *Geochem. Geophys. Geosyst.* 2,
475 2000GC000102.

476 Stroncik, N.A., Schimincke, H.U., 2002. Palagonite- a review. *Int. J. Earth Sci.* 91,
477 680–697.

478 Sumner, J.M., Blake, S., Matela, R.J., Wolff, J.A., 2005. Spatter. *J. Volcanol.*
479 *Geotherm. Res.* 142(1-2), 49–65.

480 Thorseth, I.H., Furnes, H., Tumyr, O., 1991. A textural and chemical study of
481 Icelandic palagonite of varied composition and its bearing on the mechanism of the
482 glass-palagonite transformation. *Geochim. Cosmochim. Acta* 55, 731–749.

483 Vergnolle, S., Brandeis, G., 1996. Strombolian explosions: 1. A large bubble
484 breaking at the surface of a lava column as a source of sound. *J. Geophys. Res. Solid*
485 *Earth* 101 (B9), 20433–20447.

486 Vergnolle, S., Brandeis, G., Mareschal, J.C., 1996. Strombolian explosions: 2.
487 Eruption dynamics determined from acoustic measurements. *J. Geophys. Res. Solid*
488 *Earth* 101 (B9), 20449–20466.

489 Walker, G.P.L, Croasdale, R., 1971. Characteristics of some basaltic pyroclastics.
490 *Bull. Volcanol.* 35(2), 303–317.

491 Wentworth, C.K., 1926. Pyroclastic geology of Oahu. Bernice P. Bishop. Museum,
492 Bulletin 30, Honolulu, Hawaii, 121 p.

493

494

Table 1: EDX analyses of sideromelane and palagonitized regions.

	1-palagonite Figure 4A				2-sideromelane Figure 4C					2-palagonite Figure 4D, F				3-sideromelane Figure 4B			3-palagonite Figure 4B		
N°	1	2	3	4	1	2	3	4	5	1	2	3	4	1	2	3	4	5	6
%																			
Na₂O	0.30	0.22	0.23	0.49	5.72	5.51	5.44	6.11	6.21	0.23	0.45	1.12	0.42	3.56	3.65	3.68	0.15	0.04	0.07
SiO₂	25.52	29.82	28.37	32.36	54.62	53.92	50.35	54.87	55.64	16.74	30.84	34.66	30.61	40.37	39.88	39.91	31.85	41.83	40.22
Al₂O₃	14.76	17.79	14.05	15.67	25.01	23.70	23.28	24.62	24.87	16.24	15.05	20.60	21.95	13.18	13.05	13.03	23.33	8.71	7.64
MgO	1.34	1.86	1.65	3.05	0.11	0.69	0.66	0.14	0.17	0.41	2.24	1.27	0.74	5.04	4.99	5.02	0.72	0.86	0.73
ZnO	0.00	0.02	0.00	0.19	0.07	0.04	0.00	0.04	0.02	0.00	0.00	0.00	0.00	0.09	0.01	0.00	0.03	0.07	0.00
FeO	7.41	8.23	8.60	9.58	0.93	1.26	1.24	0.74	0.82	0.33	4.59	3.18	1.06	11.47	11.48	11.43	4.34	14.93	14.10
SrO	0.00	0.00	0.00	0.00	0.01	0.04	0.05	0.04	0.01	0.02	0.16	2.60	0.30	0.00	0.00	0.00	0.00	0.00	0.00
CaO	2.21	2.18	2.94	8.20	1.63	4.18	4.44	2.11	1.07	1.74	4.26	5.27	5.58	14.72	14.51	14.49	1.53	4.37	4.43
Cr₂O₃	0.00	0.00	0.00	0.30	0.00	0.09	0.14	0.00	0.06	0.11	0.00	0.00	0.08	0.00	0.04	0.05	0.03	0.00	0.04
P₂O₅	0.54	0.47	0.20	2.30	0.38	0.87	0.19	0.83	0.09	0.48	0.83	1.16	1.90	0.80	0.88	0.83	0.33	1.11	1.24
NiO	0.05	0.02	0.00	0.01	0.00	0.02	0.00	0.00	0.02	0.00	0.01	0.03	0.02	0.00	0.00	0.00	0.04	0.00	0.03
K₂O	0.12	0.15	0.18	0.09	0.23	0.13	0.24	0.15	0.16	0.34	0.57	3.60	1.06	3.80	3.91	3.85	0.48	0.58	0.65
MnO	0.07	0.06	0.08	0.09	0.03	0.00	0.06	0.00	0.02	0.00	0.07	0.18	0.00	0.19	0.15	0.17	0.00	0.00	0.00
SO₃	0.04	0.06	0.02	0.13	0.02	0.06	0.07	0.01	0.02	0.47	0.02	0.04	0.07	0.19	0.18	0.16	0.13	0.01	0.00
TiO₂	2.51	2.66	3.97	4.79	0.36	0.42	0.53	0.39	0.49	0.17	3.48	0.29	0.28	5.84	5.82	5.80	0.28	8.17	8.15
Total	54.86	63.53	60.28	77.24	89.11	90.91	86.68	90.06	89.68	37.28	62.56	74.00	64.06	99.24	98.55	98.41	63.25	80.68	77.29

495

Table 2: Micropobre analyses with ions calculated for clinopyroxene.

	1-Diopside	2-Diopside				498
Region	Core	Edge	Interm.	Edge	Edge	Edge
%						500
SiO₂	41.33	42.79	47.36	47.41	47.30	46.41
TiO₂	6.54	5.61	2.95	3.17	3.48	5.07
Al₂O₃	9.39	8.58	4.37	5.27	5.33	5.42
FeO	7.70	7.61	7.50	6.43	6.74	7.43
MgO	10.93	11.72	16.87	13.67	13.42	15.08
MnO	0.06	0.05	0.14	0.12	0.12	0.12
CaO	23.56	23.87	21.62	23.30	23.73	23.76
Na₂O	0.43	0.46	0.29	0.29	0.32	0.35
Cr₂O₃	0.00	0.00	0.00	0.00	0.00	0.00
NiO	0.00	0.00	0.00	0.00	0.00	0.00
K₂O	0.03	0.02	0.02	0.05	0.03	0.02
Total	100.01	100.71	101.12	99.69	100.47	100.58
<i>Calculation based on 6 oxygens</i>						
Si	1.57	1.61	1.76	1.78	1.77	1.74
Ti	0.19	0.16	0.08	0.09	0.10	0.11
Al	0.42	0.38	0.19	0.23	0.23	0.24
Fe	0.25	0.24	0.23	0.20	0.21	0.23
Mg	0.62	0.66	0.93	0.76	0.75	0.73
Mn	0.00	0.00	0.00	0.00	0.00	0.00
Ca	0.96	0.96	0.86	0.94	0.95	0.95
Na	0.03	0.03	0.02	0.02	0.02	0.03
Cr	0.00	0.00	0.00	0.00	0.00	0.00
Ni	0.00	0.00	0.00	0.00	0.00	0.00
K	0.00	0.00	0.00	0.00	0.00	0.00
Ens	0.34	0.35	0.46	0.4	0.39	0.38
Fs	0.13	0.13	0.12	0.11	0.11	0.12
Wo	0.53	0.52	0.42	0.49	0.50	0.50

505 Table 3: Chemical analysis by microprobe of the spinels of the pyroclasts 1, 2 and 3.

	1				2				3		
	Fig. 4E				Fig.4G				Fig. 4H		
Region No.	Edge 1	Core 2	Edge 3	Core 4	Edge 1	Edge 2	Core 3	Core 4	Edge 1	Core 2	Edge 3
	%										
SiO₂	0.04	0.07	0.00	0.06	0.14	0.04	0.03	0.09	0.05	0.00	0.03
Al₂O₃	4.96	6.12	5.44	5.74	2.14	8.29	18.07	7.25	5.18	21.755	5.29
MgO	5.63	9.52	8.09	7.26	1,267	3.83	11.67	4.40	8.01	10.789	8.15
FeO	56.60	50.10	53.13	54.64	71.99	61.453	33.44	62.03	60.61	37.396	59.67
Cr₂O₃	0.88	6.88	6.28	2.48	3.19	5.47	2.96	8.69	1.97	20.434	3.10
MnO	0.36	0.42	0.47	0.77	0.18	0.29	4.07	0.44	0.39	0.13	0.45
TiO₂	21.77	16.70	17.74	20.18	10.392	9.12	2.30	5.34	18.94	4.65	17.93
Total	90.30	89.80	91.15	91.13	89.307	88.501	93.55	88.24	95.75	9549	95.05
<i>Calculation based on 4 oxygens</i>											
Si	0.001	0.002	0.002	0.002	0.002	0.002	0.002	0.002	0.002	0.002	0.002
Ti	0.622	0.561	0.561	0.561	0.561	0.561	0.561	0.561	0.561	0.561	0.561
Al	0.222	0.250	0.250	0.250	0.250	0.250	0.250	0.250	0.250	0.250	0.250
Cr	0.027	0.073	0.073	0.073	0.073	0.073	0.073	0.073	0.073	0.073	0.073
Fe⁺²	0.506	0.550	0.550	0.550	0.550	0.550	0.550	0.550	0.550	0.550	0.550
Fe⁺³	1.293	1.139	1.139	1.139	1.139	1.139	1.139	1.139	1.139	1.139	1.139
Mn	0.012	0.024	0.024	0.024	0.024	0.024	0.024	0.024	0.024	0.024	0.024
Mg	0.319	0.400	0.400	0.400	0.400	0.400	0.400	0.400	0.400	0.400	0.400

506

507

508

509

510

511

512

513

514

515

516

517

518

519

520

521

522

523

524

525 Table 4: Chemical analysis by microprobe of the zeolites of the pyroclast 2.

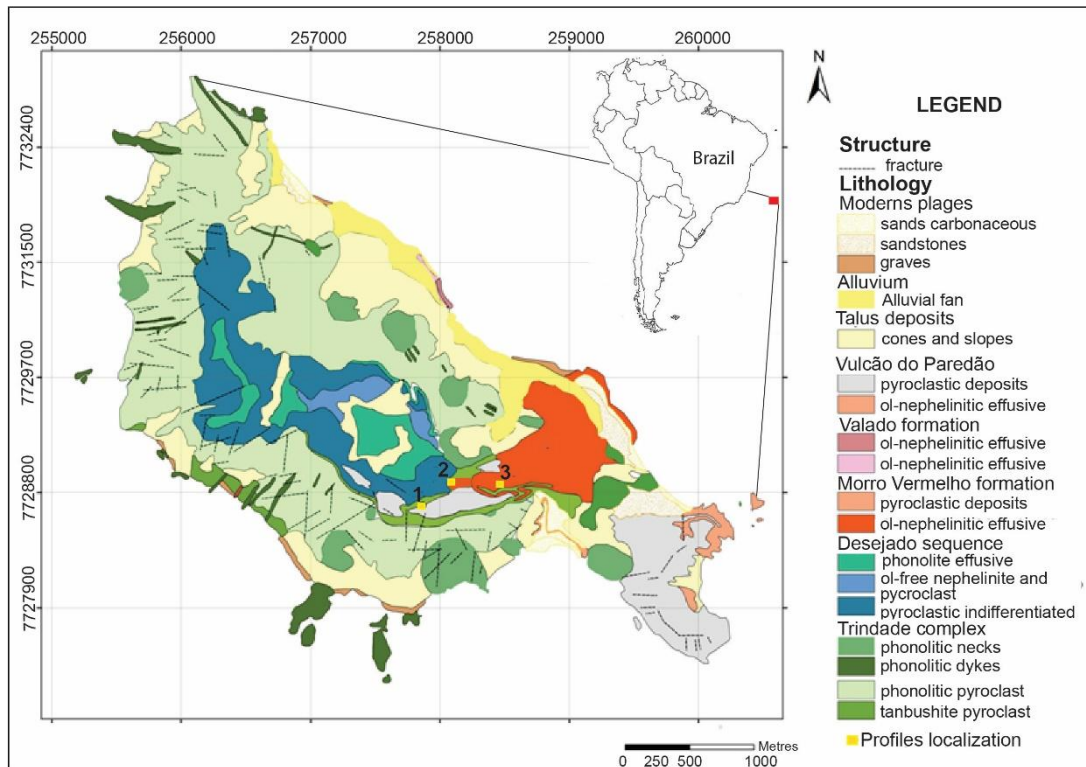
Mineral	Heulandite-Ca	Chabazite-Ca	Chabazite-Ca	Chabazite-Ca
Region	Amygdale filled Fig. 4G	Fracture Fig. 4G	Fracture Fig. 4F	Amygdale partially filled Fig. 4G
N°	5	6	5	7
%				
SiO₂	48.21	47.09	45.87	49.18
TiO₂	0.09	0.05	0.00	0.00
Al₂O₃	19.60	23.25	24.02	23.92
FeO	1.06	0.18	0.24	0.32
MgO	0.13	0.20	0.05	0.30
MnO	0.05	0.00	0.00	0.00
CaO	6.60	7.57	8.74	7.52
Na₂O	0.49	0.13	0.36	0.31
K₂O	4.24	0.69	4.98	0.91
Cr₂O₃	0.03	0.04	0.00	0.00
H₂O	19.50	20.80	14.23	17.54
Total	100.00	100.00	100.00	100.00
	<i>Calculation based on 98 oxygens</i>	<i>Calculation based on 36 oxygens</i>		
Si	21.58	7.60	8.08	8.16
Ti	0.00	0.00	0.00	0.00
Al	10.34	4.42	4.99	4.68
Fe	0.40	0.02	0.04	0.04
Mg	0.09	0.05	0.01	0.08
Mn	0.02	0.00	0.00	0.00
Ca	3.17	1.31	1.65	1.34
Na	0.85	0.08	0.25	0.20
K	4.84	0.28	2.24	0.38
Cr	0.00	0.00	0.00	0.00
H	65.50	25.18	18.82	21.84

526
527
528
529
530
531
532
533
534
535
536
537
538
539

540 Table 5: Chemical analyses of the major elements, trace and REE in representative
 541 samples of pyroclasts of the Vulcão do Paredão (1) and Morro Vermelho (2 and 3). LQ
 542 = Quantification Limit.

Pyroclasts														
%														
	SiO₂	Al₂O₃	FeO_t	TiO₂	CaO	Na₂O	K₂O	MgO	MnO	P₂O₅	LOI	K₂O/ Na₂O	Total	
1	37.47	14.68	19.58	6.95	5.43	0.53	0.15	4.50	0.30	1.36	9.05	0.28	100.00	
2	37.50	11.95	16.09	5.36	11.15	0.57	0.27	7.37	0.27	1.48	7.99	0.47	100.00	
3	37.81	13.38	18.46	7.31	3.50	0.29	0.48	3.67	0.30	0.86	13.95	1.65	100.00	
Ppm														
	As	Ba	Co	Cr	Cu	Li	Mo	Ni	Sr	Th	V	Zn	Be	Sb
1	<LQ	1377.45	127.12	252.82	44.73	14.35	<LQ	115.04	1240.76	33.40	248.97	145.55	1.08	<LQ
2	<LQ	1608.22	92.73	363.23	75.9	10.94	<LQ	127.93	1592.12	39.5	302.20	128.11	1.00	<LQ
3	<LQ	1887.55	116.35	472.19	87.47	9.69	<LQ	115.02	566.09	32.02	275.81	172.75	1.13	<LQ
	Zr	Pb	S	Sc	Ga	Y	Cd	In	Cs	La	Ce	Pr	Nd	Sm
1	314.24	<LQ	220.20	34.83	33.44	42.62	1.86	0.15	1.04	101.82	267.19	27.42	109.93	20.58
2	279.70	<LQ	110.88	29.49	28.96	48.56	0.88	0.12	0.75	124.19	299.11	32.55	131.87	24.14
3	308.19	<LQ	65.44	37.16	33.80	41.28	0.50	0.16	0.62	89.93	229.24	23.99	97.44	18.72
	Eu	Gd	Tb	Dy	Ho	Er	Tm	Yb	Lu	Tl	Pb	Bi	Th	U
1	6.34	18.01	2.00	10.1	1.67	4.03	0.46	2.56	0.35	<LQ	4.19	<LQ	8.86	2.51
2	7.28	20.60	2.25	11.26	1.87	4.66	0.53	3.04	0.41	<LQ	10.64	<LQ	11.09	2.68
3	5.85	16.37	1.87	9.67	1.64	4.04	0.48	2.68	0.36	<LQ	12.23	0,043	8.81	2.01

543
 544
 545
 546
 547
 548
 549
 550
 551
 552
 553
 554
 555
 556
 557
 558
 559
 560
 561
 562
 563
 564
 565
 566



567

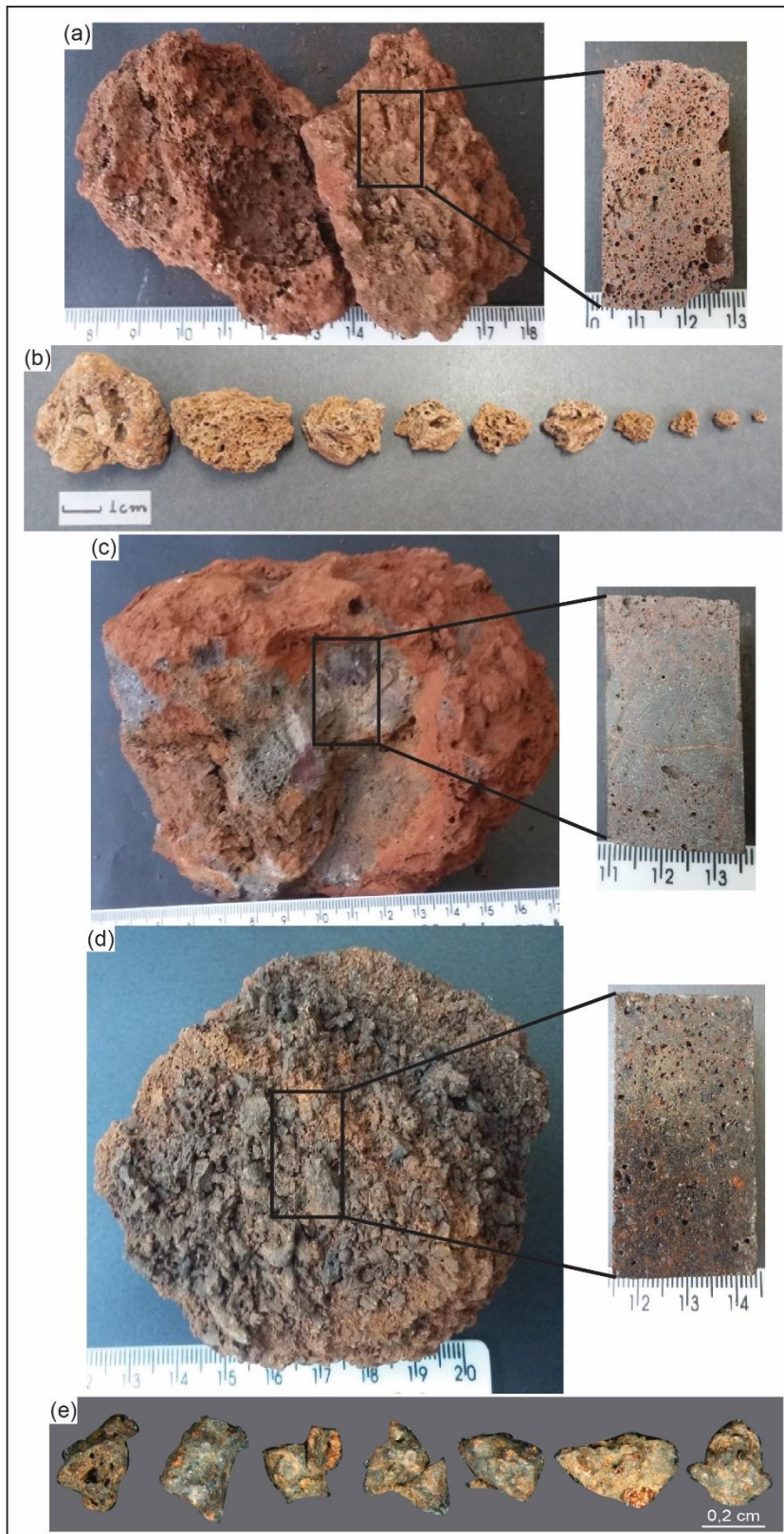
568

Figure 1: Geological map of Trindade Island and the regions of collection of pyroclasts

569

1, 2 and 3. Modified of Patrício (2012).

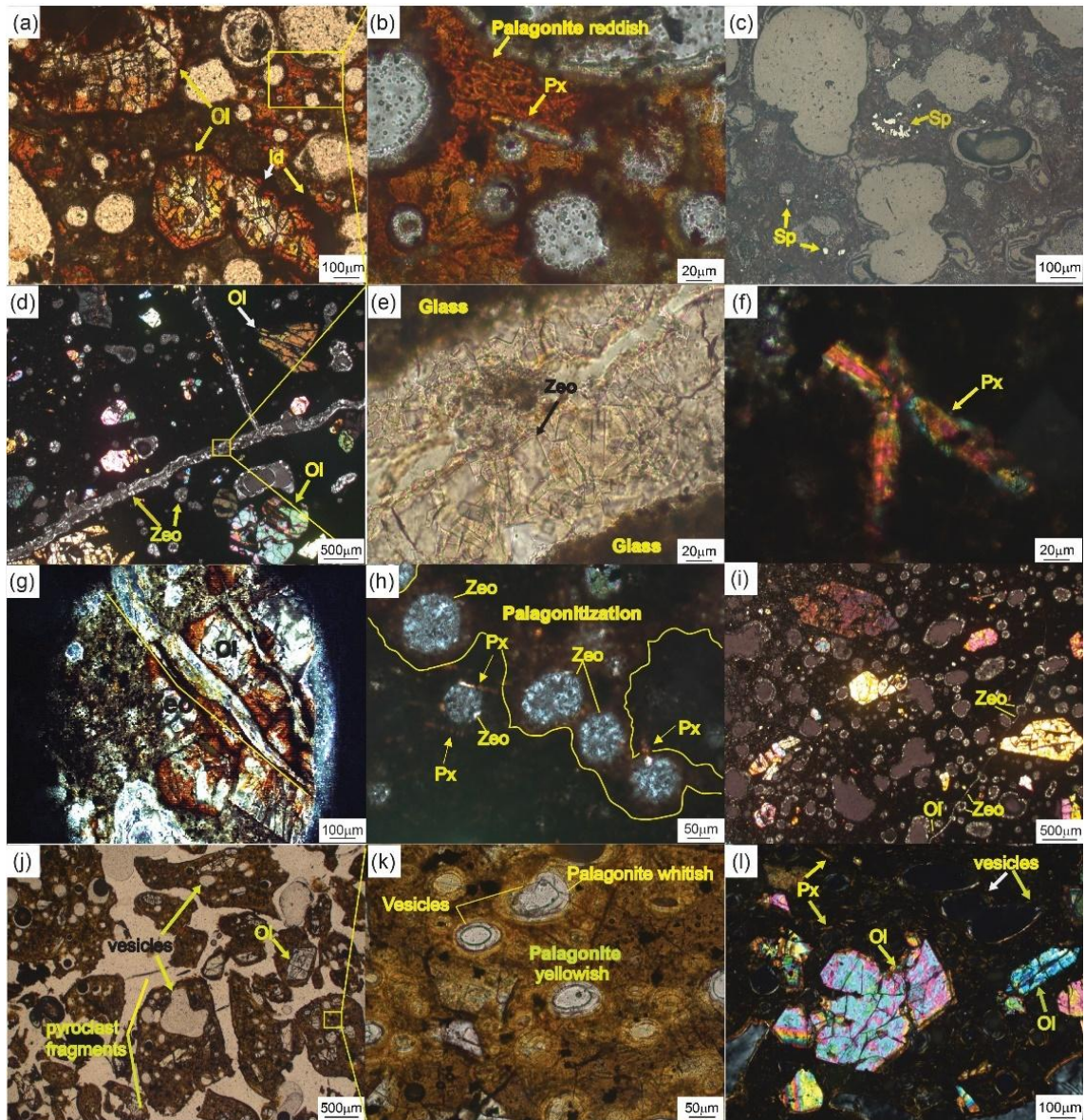
570



571
 572 Figure 2: (a) Pyroclast 1 of Vulcão do Paredão formation showing reddish-colored
 573 alteration features. On the right, sample where the blade was made for the
 574 micromorphological description. (b) Image showing lapilli of different sizes in
 575 pyroclast 1. (c) Pyroclast 2 of the Morro Vermelho formation, with the altered edges of

576 reddish coloration. On the right, image of the sample where the blade was made for the
 577 micromorphological description. (d) Pyroclast 3 of the Morro Vermelho formation. On
 578 the right is the sample where the blade was made for micromorphological description. It
 579 is possible to observe reddish-colored alteration features. (e) Image showing smaller
 580 lapilli grains of 2mm with alteration features.

581



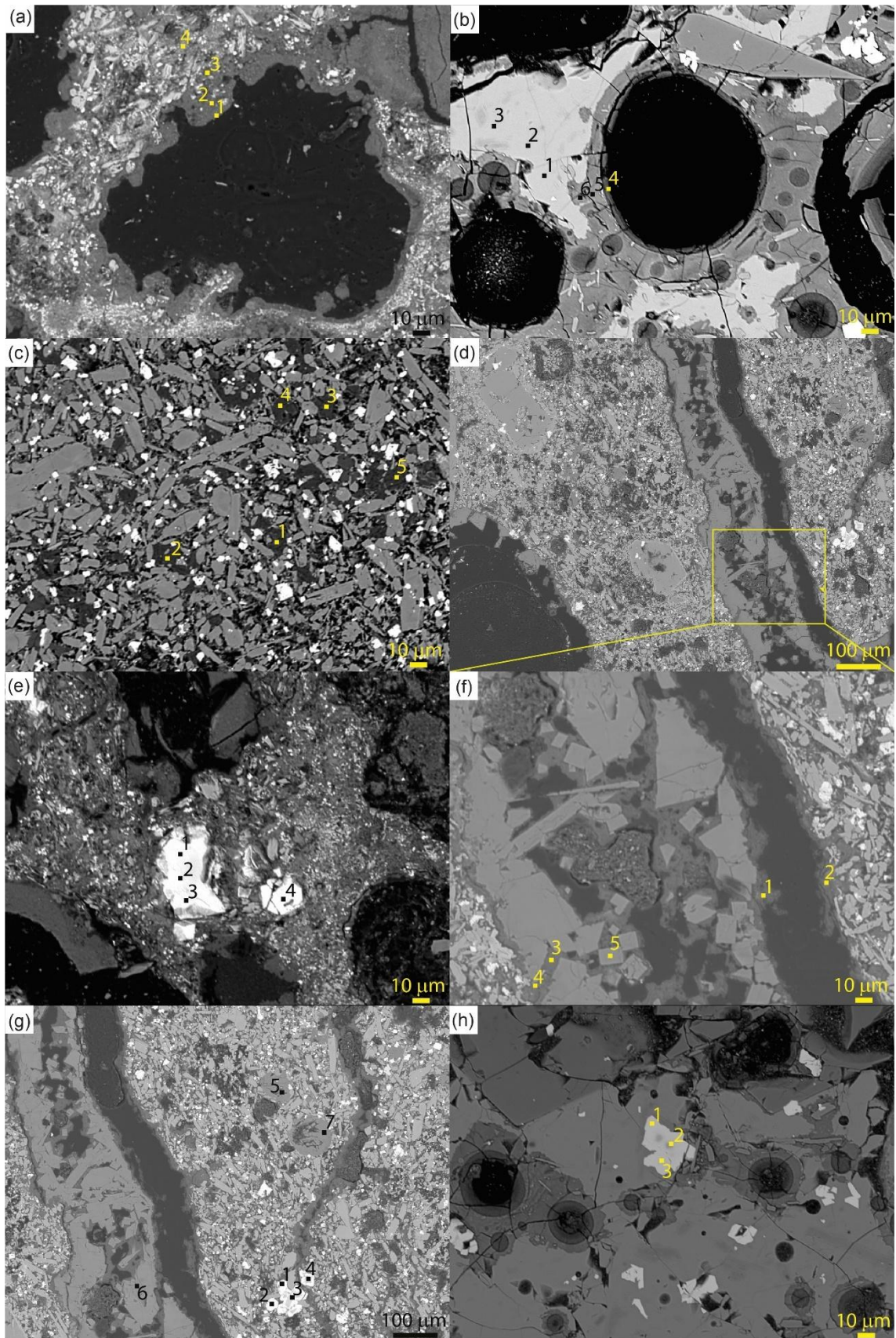
582

583 Figure 3: Pyroclast 1: (a) PPL photomicrograph from the euhedral olivine phenocrysts
 584 with altered borders for iddingsite wrapped by reddish brown matrix. (b) PPL
 585 photomicrograph from the prismatic pyroxene near vesicles wrapped in palagonite. (c)
 586 Reflected light photomicrograph showing the crystals of spinel in the matrix.

587 Pyroclast 2: (d) XPL photomicrograph showing hypocrySTALLINE structure, veins and
588 vesicles partially and totally filled by zeolites. (e) PPL photomicrograph from the
589 rhombohedral zeolites with low relief and glass volcanic grayish. (f) XPL
590 photomicrograph from the pyroxenes intercrossed. (g) PPL photomicrograph showing
591 vein of zeolite cutting olivine crystal. (h) PPL photomicrograph showing
592 hypocrySTALLINE structure and partial vesicles and fully filled by zeolites. (i) XPL
593 photomicrograph from vein of zeolite cutting vesicles filled by zeolite.

594 Pyroclast 3: (j) XPL photomicrograph from the fragments of 2mm pyroclasts with
595 vesicles structure. (k) PPL photomicrograph showing fully palagonitized glass and
596 region with white palagonite. (l) XPL photomicrograph from the hypocrySTALLINE matrix
597 with vesicles and small crystals of pyroxenes around phenocrystals of fractured
598 olivines. Some olivine crystals are euhedral. XPL = cross polarized light; PPL = plane
599 polarized light; Ol = olivine; Px = pyroxene; Sp = spinel, Zeo = zeolite.

600

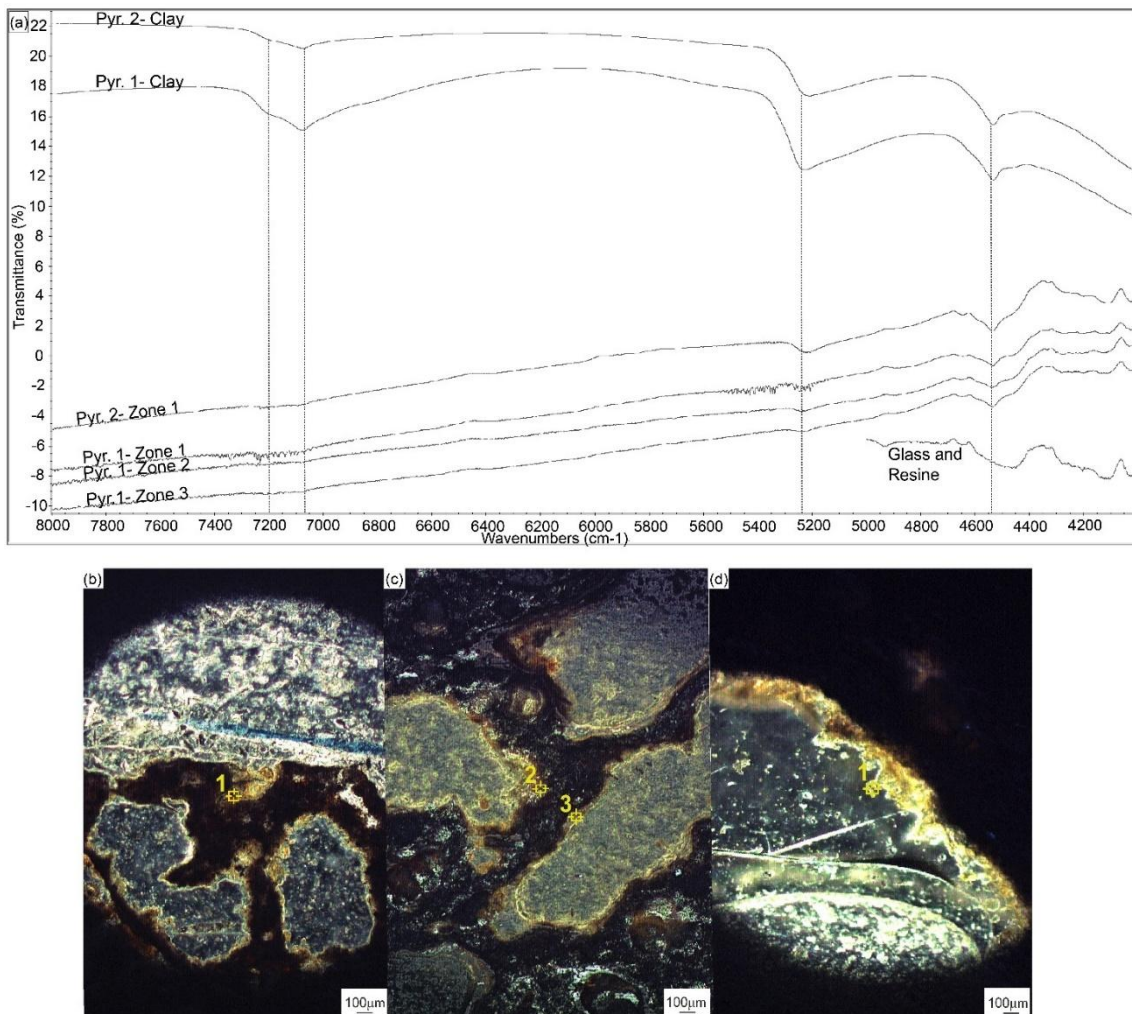


601
602
603
604

Figure 4: SEM photomicrograph and point of microchemical analyses by microprobe of pyroclasts. Pyroclast 1: (a) Punctual analysis of the palagonite in the wall and around a vesicle, (e) Punctual analysis of two spinel crystals.

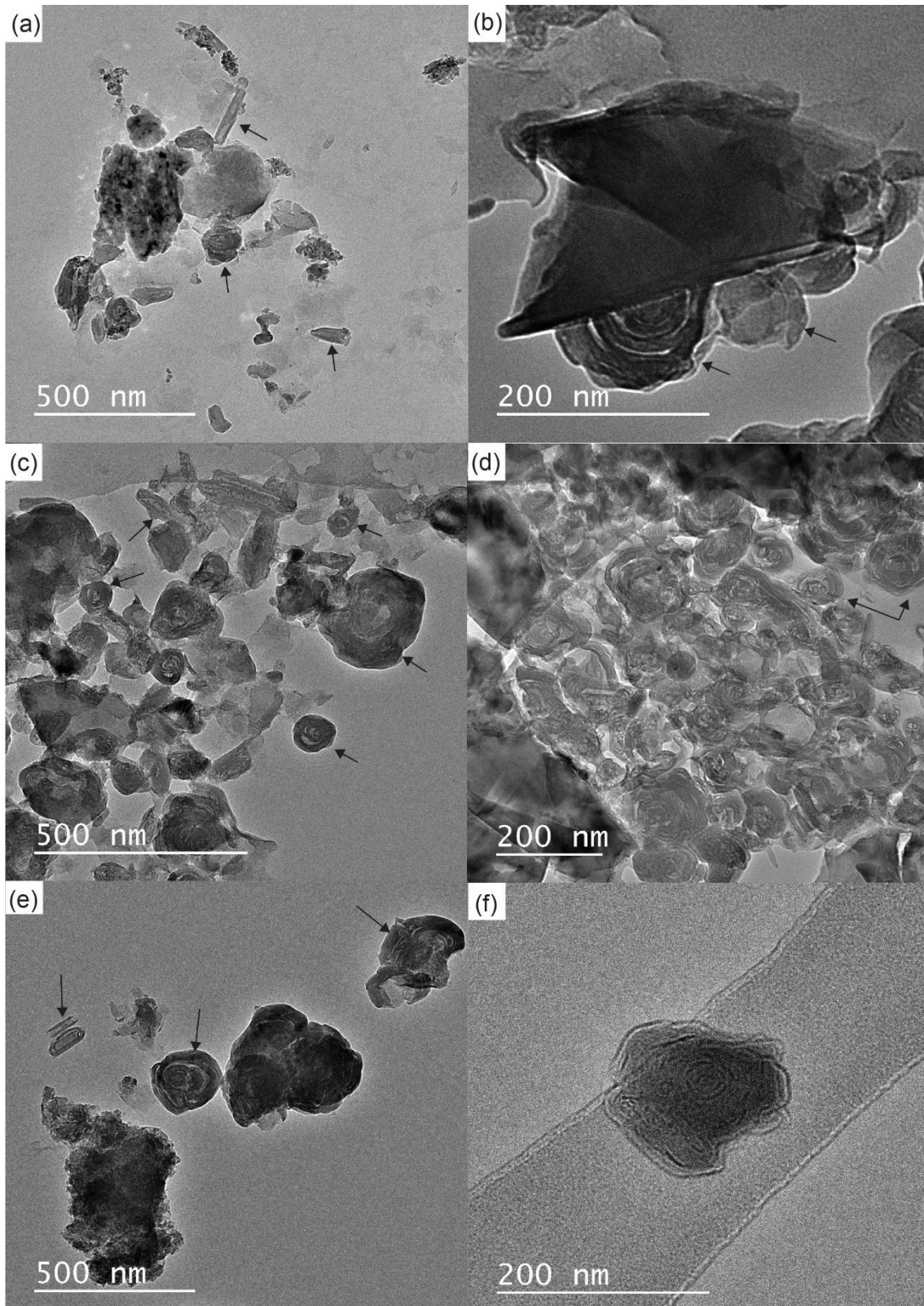
605 Pyroclast 2: (c) Punctual analyses in sideromelane in the microlytic matrix, (d) and (f)
 606 Punctual analyses in a fracture filled by zeolites and palagonite. (g) Analysis of
 607 amygdales filled by zeolites and analysis of spinels crystals.

608 Pyroclast 3: (b) Analysis of sideromelane and its alteration to palagonite., (h) Analyses
 609 of zoned spinel crystals.



610
 611 Figure 5: (a) NIR analysis of clay and palagonitized portions of pyroclast 1 and 2
 612 showing the presence of halloysite. The clay analysis was used to compare the positions
 613 of the signals between 7000 and 7230 cm^{-1} , since the signal in the palagonitized region is
 614 weak due to thickness and resin of the slender section. The spectrum of resin and glass
 615 was obtained to show the regions when occurs signal of resin and glass in spectrum of
 616 thin section. b, c and d) XPL photomicrograph in regions palagonitized and points of
 617 the analysis of the pyr. 1 (b and c) and pyr. 2 (d). Pyr=pyroclasts.

618

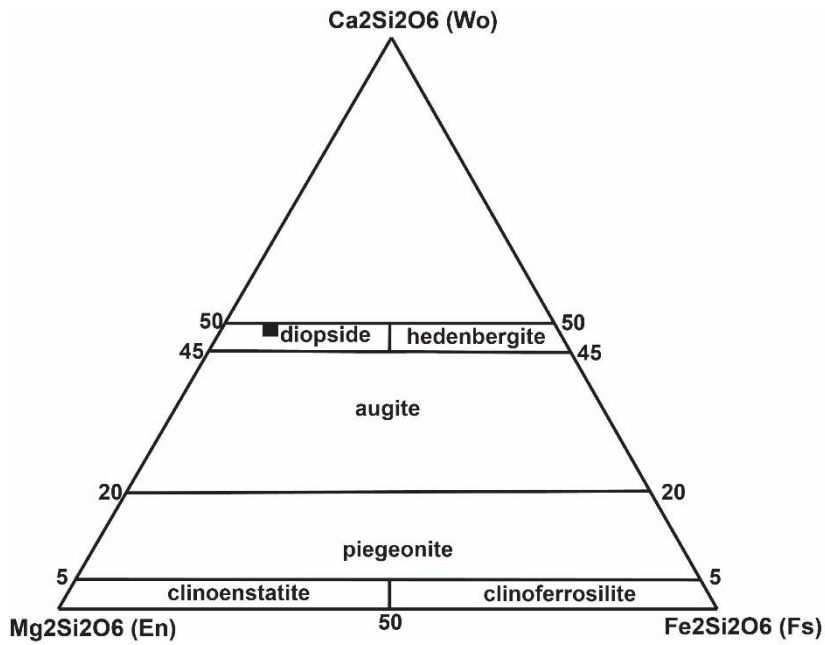


619

620 Figure 6: TEM images of halloysites in clay fraction of altered regions of the pyroclast
 621 1 (a), 2 (c), and 3 (e) and halloysites in regions with palagonitization (pyroclast 1-b, 2-d
 622 and 3-f). In all figures the arrows indicate the tubular halloysite crystals. The figure b

623 shows the fragment of volcanic glass on halloysite crystals. In the lower left corner of
624 figure d occurs a fragment of pyroxene.

625



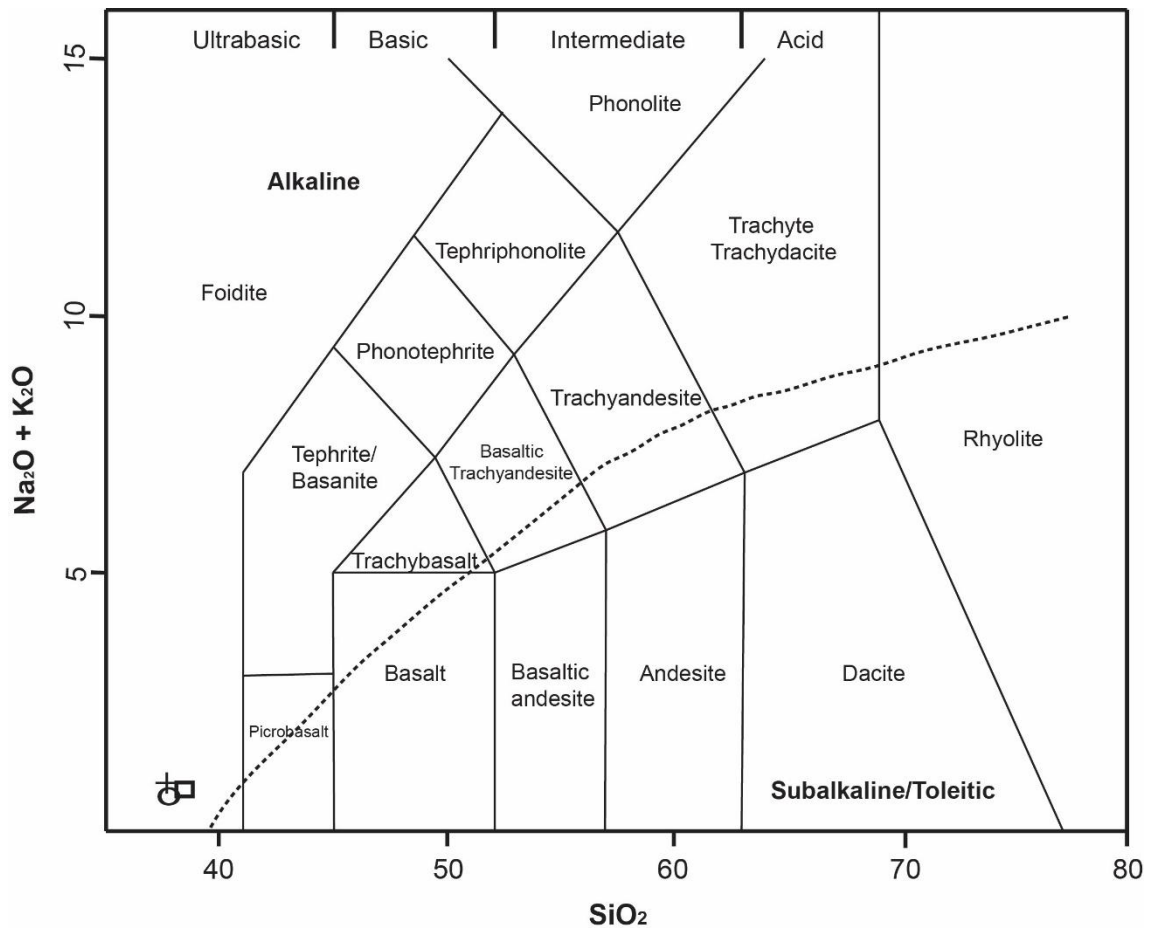
626

627 Figure 7: Morimoto diagram (1988) modified showing the composition of the
628 clinopyroxene. The square indicates the pyroclasts 1 and 2.

629

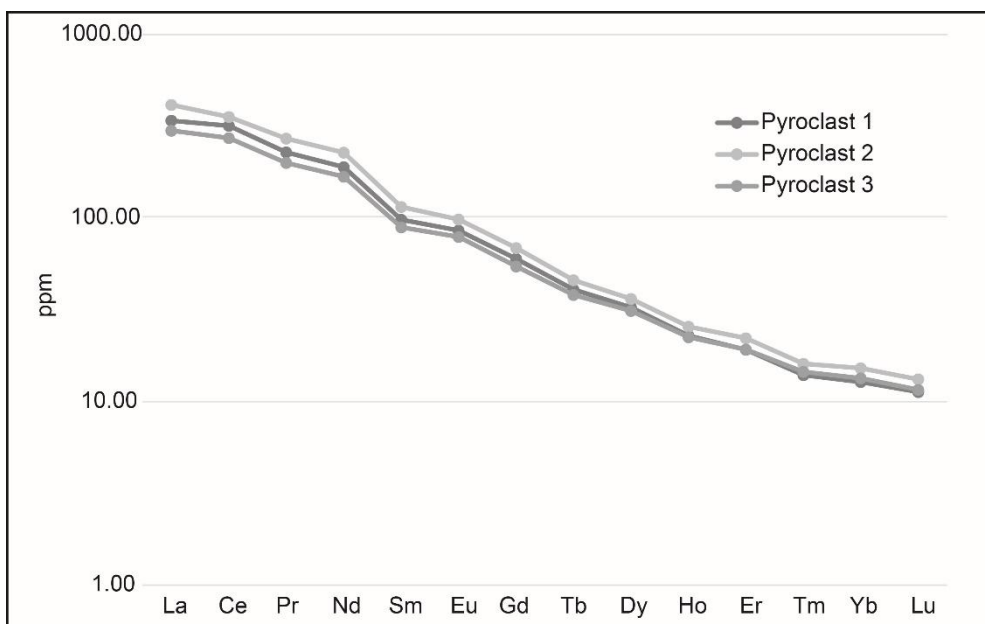
630

631



632
 633 Figure 8: TAS diagram (Les Bas *et al.* 1986) for the pyroclasts 1 (circle) of the Vulcão
 634 do Paredão and, 2 (cross) and 3 (square), both of Morro Vermelho formation.

635



636
 637 Figure 9: Typical chondrite-normalized (McDonough and Sun, 1995) rare-earth-element
 638 (REE) plots of pyroclasts.

639